Microparticle Response to Two-Dimensional Streaming Flows in Rectangular Chambers Undergoing Low-Frequency Horizontal Vibrations

Prashant Agrawal

IITB Monash Research Academy, Indian Institute of Technology Bombay, Mumbai, Maharashtra 400076, India; Department of Mechanical Engineering, Suman Mashruwala Advanced Microengineering Laboratory, Indian Institute of Technology Bombay, Mumbai, Maharashtra 400076, India and Laboratory for Micro Systems, Mechanical and Aerospace Engineering, Monash University - Clayton campus, Melbourne 3800, Australia

Prasanna S. Gandhi

Department of Mechanical Engineering, Suman Mashruwala Advanced Microengineering Laboratory, Indian Institute of Technology Bombay, Mumbai, Maharashtra 400076, India

Adrian Neild*

Laboratory for Micro Systems, Mechanical and Aerospace Engineering, Monash University - Clayton campus, Melbourne 3800, Australia

(Received 26 June 2014; revised manuscript received 21 September 2014; published 22 December 2014)

Manipulation of submicron-sized particles using second-order acoustic radiation forces at ultrasonic frequencies is hindered by the time-independent streaming flows. A similar phenomenon occurs when open fluid volumes are vibrated at low frequencies in the range of 100 Hz. The streaming phenomenon, in this lower-frequency range, is studied here by using horizontally actuated liquid-filled rectangular chambers. The formation of capillary waves at the liquid-air interface generates spatially varying flow fields in the bulk fluid, which can be used to collect particles at stable locations. However, the same spatial variation is the source of the streaming fields, which, under some conditions, can drag particles away from these stable locations. The governing equations for the second-order flow are derived and simulated, after which a particle-tracing algorithm is executed in the obtained flow field. Critical particle parameters are determined in multiple simulated chambers of different dimensions, with the aim of reducing the effect of the streaming field on the particle's movement. The simulation results are then applied experimentally to demonstrate the ability of this system to collect particles as small as 50 nm in diameter.

DOI: 10.1103/PhysRevApplied.2.064008

I. INTRODUCTION

Recent developments in lab-on-a-chip microfluidic systems have triggered research into particle manipulation for applications including sensing, collection, and sorting in a variety of systems. In this context, mechanical vibrations have been studied due to advantages such as ease of integration and application to a wider particle range than other noninvasive methods, such as dielectrophoresis [1] and optical [2] and magnetic [3] tweezers. Particle manipulation via mechanical vibrations can be further divided into two distinct frequency regimes: high-frequency (ultrasonic) actuations (in the range of megahertz) and low-frequency actuations (in the range of 100 Hz).

In the high-frequency regime, particle motion is caused by ultrasonically generated forces comprising of (i) acoustic radiation force, (ii) drag force due to acoustic streaming, and (iii) Bjerknes forces. All these forces are second order, meaning that while the ultrasonic field is oscillating at high frequency, these forces when time averaged over an oscillatory cycle are nonzero and, hence, act as if steady state. The acoustic radiation forces originate because of the scattering of acoustic waves on the particle surface, acoustic streaming results from body forces acting directly on the vibrating fluid, and Bjerknes force is a form of interparticle acoustic radiation force that arises from the scattering of acoustic waves from the surface of other nearby oscillating particles [4]. The acoustic radiation force causes particles to migrate (over thousands of cycles) towards the pressure nodes or antinodes, depending on their acoustic contrast factor. The acoustic radiation force has been analytically formulated [5,6] and, subsequently, has been used to manipulate particles for applications in flowing [7–10] and in stationary fluid volumes. In closed microfluidic systems, it has been used to collect particles in lines [11,12], 2D arrays [13,14], and 3D cages [15] and manipulate particles in the form of acoustic tweezers, through phase control [16] and mode switching [17,18]. In open fluid volumes, it has been used to collect particles in drops [19] and films [20].

*Corresponding author.
adrian.neild@monash.edu

Acoustic streaming originates because of spatial variations in the velocity field of the vibrating fluid. As a result, the time average of the momentum flux terms in the Navier Stokes' equation is nonzero which acts directly as a body force on the fluid and, therefore, indirectly as drag on the particle [21]. Acoustic streaming is observed as rotational patterns and primarily occurs in three forms: (i) Schlichting streaming, which is generated at the viscous boundary layer, (ii) Rayleigh streaming, which are bulk flows driven by the Schlichting vortices, and (iii) Eckart streaming, which is generated due to acoustic energy attenuation in the bulk of the fluid [22]. Of these, in general, Eckart streaming is less dominant in microfluidics systems but, rather, is apparent in systems of the order of a millimeter or longer [23]. Acoustic streaming fields are numerically studied in the perpendicular plane [24], as well as within the plane of the transducer [25] and, more recently, in three dimensions [26,27]. It has primarily found applications in acoustic mixing [28,29] but poses a hindrance for particle collection in most systems [30], and, therefore, strategies for reducing or controlling streaming have been explored [13,31]. Nevertheless, streaming has found applications in sorting particles in conjunction with acoustic radiation forces [32–34].

Hence, particle movement in the ultrasonic regime has been thoroughly studied and implemented in microfluidic systems with impressive control over particle trajectory. In comparison, however, the low-frequency regime is much less explored. Particle collection in the form of ripples in closed systems through pulsating fields has been demonstrated [35–37], while in open systems particle movement is triggered by the formation of capillary waves at the liquid-air interface, causing floating particles to accumulate at the nodes and antinodes of the capillary wave, depending on their hydrophobicity [38], and sedimented particles to be collected due to inertial effects at locations dictated by the gradient of the flow field in rectangular chambers [39,40] and in droplets [41].

The spatial variation of the flow field under the capillary waves and the gradients arising due to viscosity will generate streaming flows in this frequency regime as well [42]. In this work, we characterize these low-frequency streaming flows through numerical modeling of the flow in horizontally actuated rectangular chambers. Here, the key difference with ultrasonic systems is that these low-frequency vibrations produce much larger boundary-layer thicknesses, which are comparable to the chamber height. This distinction is important, as it is found that submicron-sized particles can be collected at lower liquid-volume heights [43].

A perturbation scheme is used to formulate the governing equations for this second-order flow, on the lines of the formulation presented by Nyborg in the acoustic domain [21]. Particle motion is studied, and, subsequently, critical particle properties are determined, based on their tendency to get trapped in the streaming vortices or get collected in stable locations. The trajectory analysis shows that, above a critical particle weight, the streaming flows assist the collection of the particles; however, below that cutoff, the streaming acts to circulate the particle continuously. Through consideration of the effect of the streaming flow, and the factors which affect its magnitude, an understanding is obtained as to which parameters determine the cutoff particle weight. This analysis is then expanded for multiple chamber dimensions, with an aim to reduce the size of particles that can be collected by the first-order fields. Indeed, through the process of streaming reduction using the simulation results, we are able to show experimentally that particles as small as 50 nm (diameter) can be collected into stable locations.

II. MODELING

A. Simulation

At the operating frequencies (less than 500 Hz) and amplitudes (less than 50 μm) used here, the flow is incompressible and laminar and, therefore, is governed by the following continuity and Navier Stokes' equations:

$$\rho_0(\nabla \cdot \mathbf{u}) = 0, \tag{1a}$$

$$\rho_0\left(\frac{\partial \mathbf{u}}{\partial t} + \mathbf{u} \cdot (\nabla \mathbf{u})\right) = -\nabla p + \mu \nabla^2 \mathbf{u} + \mathbf{f}, \tag{1b}$$

where ρ_0 is the density of the fluid, $\mathbf{u}$ is the fluid velocity vector, μ is the viscosity of the fluid, p is the pressure in the fluid, and $\mathbf{f}$ represents the body forces. On actuation, we consider small perturbations of the system from its initial state of rest; the velocity and pressure fields can be written as

$$\mathbf{u} = \mathbf{u}_0 + \mathbf{u}_1 + \mathbf{u}_2 + \cdots, \tag{2}$$

$$p = p_0 + p_1 + p_2 + \cdots, \tag{3}$$

where the subscripts 0, 1, and 2 indicate the order of the respective field, p_0 is the reference atmospheric pressure, and, as the system is initially at rest, the velocity $\mathbf{u}_0 = \mathbf{0}$. We now analyze the first- (oscillating) and second- (steady state) order fields individually by collecting the first- and second-order terms, after substituting Eqs. (2) and (3) in Eqs. (1a) and (1b).

1. Periodic first-order field (study 1)

Considering the first-order terms in Eqs. (1a) and (1b), the governing equations for evaluating the first-order fields are obtained as

$$\rho_0(\nabla \cdot \mathbf{u}_1) = 0, \tag{4a}$$

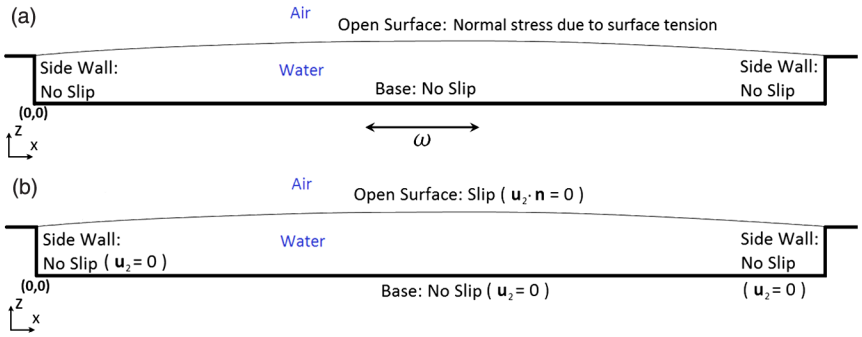

FIG. 1. Boundary conditions for the modeling of (a) a periodic first-order field and (b) a time-averaged second-order field.

$$\rho_0 \frac{\partial \mathbf{u}_1}{\partial t} = -\nabla p_1 + \mu \nabla^2 \mathbf{u}_1 + \mathbf{f}. \tag{4b}$$

At the operating vibration amplitudes, the first-order fields are linear in nature [44]. Therefore, the response to a harmonic excitation will be a harmonically varying field. A transient simulation (study 1) is performed in an open rectangular chamber, by using an incompressible laminar flow and a moving mesh algorithm in COMSOL (v4.2a). The no-slip boundary conditions for the walls are shown in Fig. 1(a), whereby the stress condition at the water-air interface, incorporating surface tension, is given as

$$\{-p_1 \mathbf{I} + \mu[\nabla \mathbf{u}_1 + (\nabla \mathbf{u}_1)^T]\} \cdot \mathbf{n} = \Gamma \gamma \mathbf{n}, \tag{5}$$

where Γ is the curvature, γ is the surface tension, $\mathbf{I}$ is a unit matrix, and $\mathbf{n}$ is the unit normal vector at the interface. For implementation, Eq. (5) is converted into its weak form and fed into COMSOL at the interface boundary. The contact line is pinned at the top edge of the side walls; this will result in a dynamic contact angle as the chamber vibrates. To simulate a chamber vibrating horizontally with amplitude A_0 and angular frequency ω, the body force $\mathbf{f}$ is implemented as

$$\mathbf{f} = -\rho_0 A_0 \omega^2 \sin(\omega t)\hat{\mathbf{i}} - \rho_0 g \hat{\mathbf{k}}, \tag{6}$$

where g is the acceleration due to gravity. Initially, a transient simulation is run on a 2D rectangular domain without any actuations to obtain the curved liquid-air interface, due to surface tension. The resulting domain is then subjected to sinusoidal horizontal vibrations to simulate the flow field, due to the standing capillary waves at the liquid-air interface. The resonant frequencies are estimated by using a 1D model for capillary gravity waves on the surface of a liquid bath with depth h [44]:

$$\omega^2 = (gk + \gamma k^3/\rho_0)\tanh(kh). \tag{7}$$

Here, k ($k = 2\pi/\lambda$) is the wave number. This model assumes the liquid to be unbounded (i.e., an infinitely wide chamber) and does not consider the effect of the side walls; as a result, Eq. (7) gives only an estimate of the resonance value. For example, for a chamber with length $L = 4$ mm and depth $h = 0.25$ mm, Eq. (7) gives a resonant frequency of 194 Hz for a capillary wave of two wavelengths. The resonant frequency in the model, for this mode, is found by performing a frequency sweep near this estimated value, keeping the base vibration amplitude constant, and finding the frequency at which the capillary wave displacement is maximum; that comes out to be close to 220 Hz.

The simulation is performed for a considerable number of cycles to ensure that the liquid field's periodicity has been established. Further analysis, for the second-order fields, is performed on one cycle of this periodic first-order field.

2. *Time-averaged second-order field (studies 2 and 3)*

Considering the second-order terms, after substitution of Eqs. (2) and (3) in Eqs. (1a) and (1b), the second-order flow field will be governed by

$$\nabla \cdot \mathbf{u}_2 = 0, \tag{8a}$$

$$\mu \nabla^2 \mathbf{u}_2 = \nabla p_2 + \rho_0[(\mathbf{u}_1 \cdot \nabla)\mathbf{u}_1 + \mathbf{u}_1(\nabla \cdot \mathbf{u}_1)] + \rho_0 \frac{\partial \mathbf{u}_2}{\partial t}. \tag{8b}$$

For the considered amplitude ranges in our analysis, the capillary wave amplitude is about 2 orders smaller than the capillary wavelength. In such a scenario, the velocity field response can be considered to be linear [44]. This result implies that the magnitude of the higher-order velocity fields will be negligible compared to the first-order response. Following this, the dynamic second-order term on the right side of Eq. (8b) is neglected and only the steady second-order effects are analyzed through the equations

$$\nabla \cdot \langle \mathbf{u}_2 \rangle = 0, \tag{9a}$$

$$\mu \nabla^2 \langle \mathbf{u}_2 \rangle = \nabla \langle p_2 \rangle - \mathbf{F}. \tag{9b}$$

Here $\langle x \rangle$ represents the time-averaged value of the field variable x. The source term $\mathbf{F}$, which drives this second-order field, is given by

$$\mathbf{F} = -\rho_0 \langle (\mathbf{u}_1 \cdot \nabla)\mathbf{u}_1 + \mathbf{u}_1(\nabla \cdot \mathbf{u}_1) \rangle. \tag{10}$$

As the first-order fields are harmonic in nature, the product of first-order quantities (in $\mathbf{F}$) will result in terms which oscillate with twice the frequency and also terms which are constant in time. By time-averaging Eqs. (8a) and (8b), the time-dependent part is reduced to zero and only the steady part is extracted. To find the source term $\mathbf{F}$ by using COMSOL, a separate transient study (study 2) is performed over one cycle; this study is in continuation to study 1, which establishes the first-order fields. In study 2, the first-order fields are calculated simultaneously with a partial differential equation, which solves for $\mathbf{F}'$ as follows:

$$\frac{2\pi}{\omega}\frac{\partial \mathbf{F}'}{\partial t} = -\rho_0[(\mathbf{u}_1 \cdot \nabla)\mathbf{u}_1 + \mathbf{u}_1(\nabla \cdot \mathbf{u}_1)]. \tag{11}$$

At the end of the cycle, the solution of Eq. (11), i.e., $\mathbf{F}'$, will be equal to $\mathbf{F}$. It is to be noted that the first-order field calculations in this study are continued from the results of study 1. Finally, the obtained value of $\mathbf{F}$ is fed into a stationary laminar flow model (study 3) as a body force, which solves for $\langle \mathbf{u}_2 \rangle$ through Eqs. (9a) and (9b). The boundary conditions for this study are shown in Fig. 1(b).

A mesh convergence analysis is performed for the $\mathbf{u}_1$ and $\langle \mathbf{u}_2 \rangle$ fields by using a parameter C_1 defined through Eq. (12):

$$C_1 = \sqrt{\frac{\int (x - x_{\mathrm{ref}})^2 dydz}{\int x_{\mathrm{ref}}^2 dydz}}. \tag{12}$$

Here, x_{ref} is the value calculated for the flow-field variable x at the mesh size ratio $d_{\max}/\delta = 0.05$, which is taken as the reference mesh size; $d_{\max}$ is the maximum element size for the mesh in the bulk of the domain, and δ is the boundary layer thickness. The plot of C_1 for different mesh sizes is shown in Fig. 2. Considering the computation time and the accuracy of the results, the limiting value of C_1 is taken to be 0.001. Accordingly, the maximum mesh size used in the bulk of the computation domain is $d_{\max} = 0.15\delta$ and a finer mesh of size $0.2d_{\max}$ at the base where particles traverse.

The first- and second-order velocity fields obtained from study 2 and 3, respectively, are extracted from COMSOL and fed into MATLAB to characterize particle motion.

3. Particle-tracing algorithm

The final velocity field acting on the particles is be given as

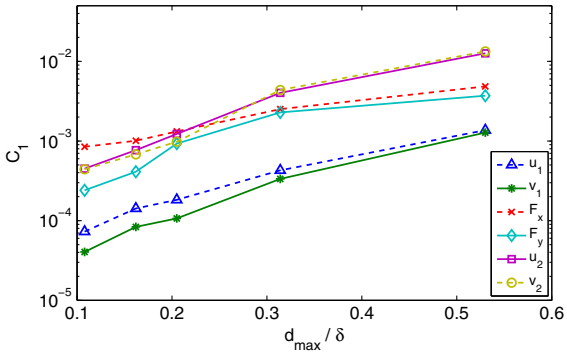

FIG. 2. Semilogarithmic plot of the convergence parameter C_1 for the different field variables for varying mesh sizes. The limiting value of C_1 is taken to be 0.001 to balance the computation time and the accuracy of the results

$$\mathbf{u} = \mathbf{u}_1 + \langle \mathbf{u}_2 \rangle. \tag{13}$$

The velocity fields are extracted at positions relative to the moving chamber, but their numeric values are absolute, i.e., with respect to a fixed global reference frame. $\mathbf{u}_1$ is extracted over one cycle (from study 2) and then superimposed with $\langle \mathbf{u}_2 \rangle$ (from study 3), as per Eq. (13) at each time instant. Particle motion is then traced by subjecting the particle to this net field repeatedly, thereby replicating the effect of an oscillating flow field. As the amount of data that can be processed is limited, bilinear interpolation is used to increase the spatial and temporal resolution of the velocity field.

Particle motion in this accelerated flow field is affected by the following forces [45]:

(i) viscous drag forces (given by the Khan and Richardson expression for $\mathrm{Re}_p > 0.01$ [46]):

$$\mathbf{F}_v = \pi r^2 \rho_0 |\mathbf{u} - \mathbf{u}_p|(\mathbf{u} - \mathbf{u}_p) \times [1.84\mathrm{Re}_p^{-0.31} + 0.293\mathrm{Re}_p^{0.06}]^{3.45}; \tag{14a}$$

(ii) force due to pressure stresses on the particle surface:

$$\mathbf{F}_p = \rho_0 V \dot{\mathbf{u}} - (\rho_p - \rho_0) V g \hat{\mathbf{k}}; \tag{14b}$$

(iii) virtual mass force ($\mathbf{F}_{\mathrm{VM}}$):

$$\mathbf{F}_{\mathrm{VM}} = \frac{\rho_0 V}{2}(\dot{\mathbf{u}} - \dot{\mathbf{u}}_p), \tag{14c}$$

where $\mathbf{u}_P$ is the particle's velocity, r is the particle radius, ρ_p is the particle density, V is the volume of the particle, and Re_p is the corresponding particle Reynold's number ($\mathrm{Re}_p = \rho_0 |\mathbf{u} - \mathbf{u}_p| 2r/\mu$). Another force, termed as the Basset (or history) force, also exists due to unsteady

viscous stresses on the particle's surface, but it is neglected here as the relative acceleration of the solid particle is very small compared to that of the liquid [45]. The forces are assumed to be acting at the center of the particle, which is taken to be, initially, at a distance equal to the radius r above the base. The presence of particles is assumed to have no effect on the flow field, and the particle is assumed to be unaffected by the hydrodynamic interactions at the wall [47]. Therefore, the particles are assumed to undergo only a translation motion, without any rotation.

B. Experimental setup

The experimental setup consists of rectangular chambers of two different chamber dimensions ($L \times W \times h$): 4 mm × 5 mm × 0.25 mm and 8 mm × 2 mm × 0.1 mm. The reason for choosing these chamber dimensions will be explained through simulations in Sec. II A. In these chambers, the length dimension L, i.e., the 4- and 8-mm edge, is taken as the principle edge along which the capillary waves are actuated; thus, due to the nature of actuation, the width of the chamber does not affect the particle motion. These chambers are mounted on a glass slide and vibrated horizontally by an electromagnetic shaker (Brüel and Kjaer, LDS, model V201), as shown in Fig. 3. Polystyrene particles (particle diameters ranging from 50 nm to 1 μm) and silica particles (particle diameter = 1 μm) are inserted with water as the base fluid in the chamber. A signal generator (Stanford Research SDR 345) actuates the shaker via a power amplifier (Brüel and Kjaer, LDS, model PA 25E). The collection is captured by using a CCD camera (Hitachi, KP-D20AU) connected to a magnification lens (InfiniVar Video Microscope, Infinity Photo-Optical Co.) with a light source (Fiber-Lite, model MI-152); the images are recorded at 29 frames per second with a video capture card (Leadtek Winfast VC100U).

It is to be noted that the actuation accelerations employed in the experiments are well below the threshold acceleration above which Faraday instability is observed; this threshold acceleration is given by [48]

$$a_c = 8\left(\frac{\rho_0}{\gamma}\right)^{1/3}\frac{\mu}{\rho_0}(2\omega)^{5/3}. \tag{15}$$

III. RESULTS AND DISCUSSION

A. Simulation

In this section, the system will be analyzed through a series of simulations, the key aims being to elucidate the mechanics behind the collection and parameters at which streaming flows prevent collection. The result is the capability to predict a cutoff criterion, on one side of which the particles will be collected into lines and, on the other side, will circulate in the streaming flow. While these criteria are obtained by modeling the full system, it is practical to describe the mechanisms on a simplified system. This simplified system assumes a fluid volume with a flat water-air interface and a defined fluid flow profile based on approximate analytical solutions, which assumes an infinite chamber length and finite depth. It is important to note that the chamber depth should be such that the capillary waves can interact with the Stokes' boundary layer from the base, to generate the desired flow field capable of collecting particles [39].

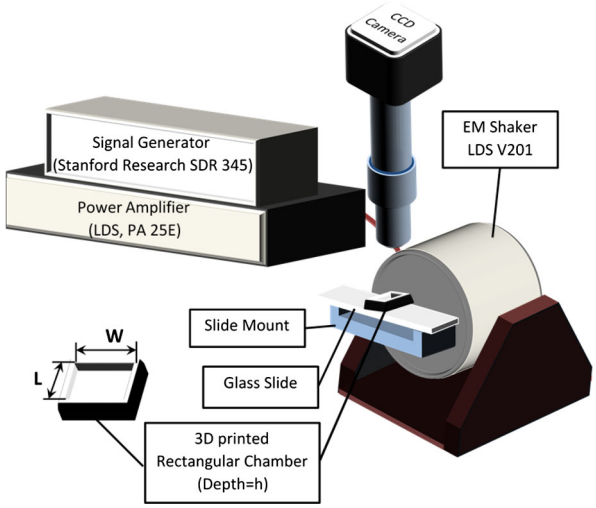

FIG. 3. A diagrammatic representation of the experimental setup for low-frequency horizontal actuations. A chamber of length L, width W, and depth h is used for collecting particles.

It is to be noted here that, in the following discussions, the $\mathbf{u}_1$ field in the x and z directions will be represented as u_1 and w_1, respectively, and the $\langle \mathbf{u}_2 \rangle$ fields in the x and z directions will be represented as u_2 and w_2, respectively.

1. Particle motion due to first-order field

We first consider the effect due to the first-order fluid flow only. In the simplified model, the first-order flow field in a horizontally actuated chamber can be approximated by the superposition of the field due to the Stokes' boundary layer on an oscillating plate [44] and the field under a capillary wave [49]. The field under a capillary wave is defined in line with our simplified model, i.e., in a chamber of infinite length and a finite depth. The superimposed first-order flow velocities are given by the equations

$$u_1 = A_0\omega e^{-\beta z}\cos(\omega t - \beta z) + u_0\cos(kx)\left(\frac{-k\sinh(kz)}{\beta\sqrt{2}}\cos(\omega t - \pi/4) + \cosh(kz)\cos(\omega t) - e^{-\beta z}\cos(\omega t - \beta z)\right), \tag{16a}$$

$$w_1 = u_0 \sin(kx)\left(\frac{-k\cosh(kz)}{\beta\sqrt{2}}\cos(\omega t - \pi/4) + \sinh(kz)\cos(\omega t) + \frac{ke^{-\beta z}}{\beta\sqrt{2}}\cos(\omega t - \beta z - \pi/4)\right). \quad (16b)$$

Here, $\beta = \sqrt{\omega\rho_0/2\mu}$ is the Stokes' boundary layer coefficient, $k = 2\pi/\lambda$ is the wave number, and u_0 is the corresponding flow magnitude. By using approximate values, the respective flow fields (plotted, but not modeled, by using COMSOL) are shown in Figs. 4(a) and 4(b). In these plots, the nodes on the capillary wave are identified by the positions of zero vertical displacement (i.e., zero w_1 velocity) on the interface.

The drag due to these spatially varying fields forces the particles to move towards the region of slower flow, which in this case corresponds to the locations A, B, and C, i.e., beneath the alternate nodes [39]. To elaborate on this mechanism, we consider a sediment particle at position P in a field with horizontal flow velocity varying as $u_f(x,z)\cos(\omega t)$ (this is representative of the conditions at a very small distance above the base of the chamber). It is seen from Fig. 4(a) that the flow-field magnitude [i.e., $u_f(x,z)$] close to the base decreases from P to B. The solid particle's motion is visualized relative to the motion of a fluid particle at P (the motions differ due to inertia), to ascertain the relative strength of the flow that the particle experiences during a cycle. To establish a qualitative understanding for this process, we split the particle's motion into four time intervals of $T/4$ each as shown in Fig. 5(a) and assess the average values of u_f experienced by the particle, in each of the time intervals.

Drag on the solid particle is proportional to the flow-field velocity observed by it; therefore, it can be intuitively said that the particle's net displacement will be proportional to the sum of u_f in each of the intervals. Taking the flow direction into account, this result can be expressed as

$$\Delta x_P \propto (u_{f1} - u_{f2} - u_{f3} + u_{f4}), \quad (17)$$

where Δx_P is the displacement of the particle over a given cycle and u_{f1}, u_{f2}, u_{f3}, and u_{f4} are the flow-field amplitudes experienced by the particle in their respective time intervals. For the trajectory in Fig. 5(a), whenever the solid particle is in the region leftward of the fluid particle, it experiences a stronger flow field than when it is rightward of it. Taking this into account, the following inequality for the flow-field strengths can be written based on the particle's position in each of the time intervals:

$$u_{f1} > u_{f2} > u_{f3} \approx u_{f4}. \quad (18)$$

The inequalities in expression (18) will result in a positive value for the particle's displacement (Δx_P) over a cycle [Eq. (17)]; i.e., the particle will move towards B. Therefore, over multiple cycles, particles will accumulate in the region of slowest fields, which corresponds to A, B, and C in Fig. 4(a).

The above mechanism is driven by the phase lag between the solid and fluid particle due to the solid particle's inertia; higher inertia causes an increase in the displacement per cycle [39]. In other words, it can be said that a particle with lower inertia will tend to diverge from the fluid particle's motion by a lesser degree. This inertial property plays a critical role when particle motion in the presence of streaming fields is considered, as will be explained in the following sections.

2. *Particle motion with the inclusion of streaming field*

We have seen how particles will move in response to the first-order fluid fields only; however, in reality, the streaming field will always be present. So we now consider the additional effects that arise from streaming, again by the use of our simplified model of a fluid in a chamber, with a flat interface with an infinite length and finite depth.

The u_2 and w_2 streaming fields, governed by Eqs. (8a) and (8b), are shown in Figs. 4(c) and 4(d). Close to the base, it is seen that the u_2 field [Fig. 4(c)] is directed towards all the nodes, and the w_2 field is positive and maximum at the nodes A, B, and C. This result hints at a behavior in which certain particles will be collected underneath all the nodes and other smaller particles will circulate

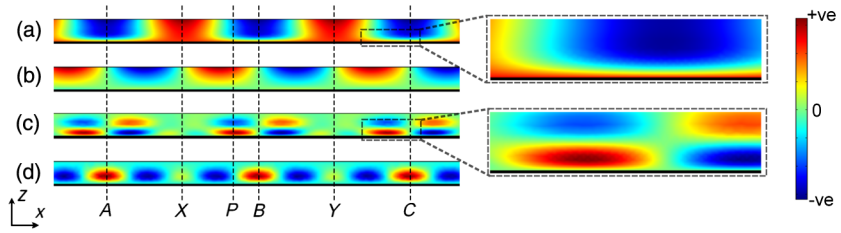

FIG. 4. First- and second-order fields in a horizontally actuated chamber plotted in COMSOL by using Eqs. (16a) and (16b): (a) u_1, the magnified view of the flow field near the base at C (or A, B) is shown in the inset; (b) w_1; (c) u_2, the magnified view of the flow field near the base at C (or A, B) is shown in the inset; (d) w_2. The first-order fields are shown at time $t = 0$. The values of u_0 and A_0 are approximated, while ω and k are approximately identified based on the wavelength in the chamber.

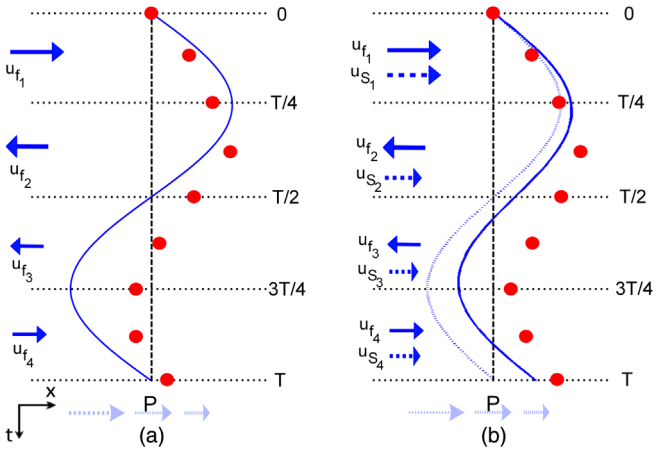

FIG. 5. Particle movement (red circles) relative to a fluid movement (solid blue line) at P in a horizontally actuated chamber: (a) first-order field only; (b) first-order field with a streaming field. The faded arrows (bottom) depict the spatially varying fluid field around P; such a variation signifies that a fluid particle left or right of P will move faster or slower than this, respectively. The velocity arrows on the left, in the respective figures, indicate the average first-order flow-field strengths experienced by the particle over each quarter of a cycle. The dotted arrows on the left in (b) indicates the strength of the second-order field in the respective time intervals. The dashed curve in (b) represents the fluid motion without the streaming field.

due to streaming [see Fig. 6(c), which shows motion of such particles in the full simulated field]. We distinguish between this behavior later; however, at this stage of the analysis, the particle sizes considered are restricted to those that do not undergo any vertical displacement over a cycle. The particles may get momentarily dislodged from the base during their motion [as in Fig. 6(d)], but their net vertical displacement over one cycle is zero.

Because of the first-order fields, particles diverge from the nodes X and Y and move towards A, B, and C. Therefore, according to the direction of the u_2 field, except for the region close to X and Y, particle movement (in the x direction) towards the nodes A, B, and C is enhanced by the u_2 streaming fields. With the added u_2 field, the displacement of a particle at P can be represented as

$$x_P \propto (u_{f_1} - u_{f_2} - u_{f_3} + u_{f_4}) + c(u_{S1} + u_{S2} + u_{S3} + u_{S4})/4, \tag{19}$$

where c is a constant which signifies the relative contribution of the streaming field in the particle's total displacement and u_{S1}, u_{S2}, u_{S3}, and u_{S4} are the average value of the u_2 field experienced by the particle in the respective time intervals [Fig. 5(b)]. As with u_f, the above values for the streaming field will be different in each of the intervals, but their direction in each time interval is the same. The particle's modified motion in the presence of a streaming field is shown in Fig. 5(b).

Particle motion in the x direction.—Having analyzed the motion of particles under the effect of the total field along the base by using a simplified model, we now examine the contribution of streaming, and its effect with varying particle inertia, on the particle's displacement over a cycle. This analysis uses data from COMSOL simulations of a realistic chamber of finite length and curved upper surface (as described in the simulation Sec. II A). The following data correspond to a water-filled chamber, of dimensions $(L, h) = (4\text{ mm}, 0.25\text{ mm})$, vibrating horizontally with two capillary wavelengths at the interface with an amplitude of 20 μm at 220 Hz.

It was mentioned in Sec. III A 1 that, with a decrease in particle inertia, the phase lag between the solid and fluid particle's motion decreases; i.e., the particle tends to follow the fluid motion closely. Therefore, it is important to assess the contribution of a streaming field in a particle's displacement with varying particle inertia. To do so, we compare the drag force due to streaming in the x direction ($F_{x\text{str}}$) and employ the concept of equivalent force (F_{eq}), which would reflect the particle's total displacement in the x direction over one cycle (as a combined result of streaming and first-order effects). This equivalent force is defined in an alternate system as the force experienced by the particle in a stationary fluid, which imparts the same displacement to the particle as it experiences in the simulated flow field [40]; this is represented in Fig. 6(e). The acceleration of the particle in this system will be equal to the total force, i.e., the difference of the equivalent force on the particle and the opposing drag due to the stationary fluid. To find this equivalent force, the particle's displacement over two cycles is considered in Fig. 6(d). The equivalent force on the particle at point P is given by

$$F_{\text{eq}} = 6\pi\mu r v_c + \frac{4}{3}\pi r^3 \rho_p a_c. \tag{20}$$

Here, $6\pi\mu r v_c = F_{\text{drag}}$ in Fig. 6(e), v_c is the average velocity of the particle, i.e., $v_c = (v_1 + v_2)/2$, where v_1 and v_2 are given by

$$v_1 = \frac{x_P - x_1}{1/f}, \qquad v_2 = \frac{x_2 - x_P}{1/f}, \tag{21}$$

and a_c is the average acceleration [$a_c = (v_2 - v_1)/(1/f)$]; f is the vibration frequency. The drag due to streaming is calculated by

$$F_{x\text{str}} = 6\pi\mu r u_S, \tag{22}$$

where u_S is the u_2 field on the particle at point P. A ratio of these forces, $R_x = F_{x\text{str}}/F_{\text{eq}}$, is employed to estimate the role of streaming in the particle's motion over a cycle for different particle radii [Fig. 7(a)] and density [Fig. 7(b)].

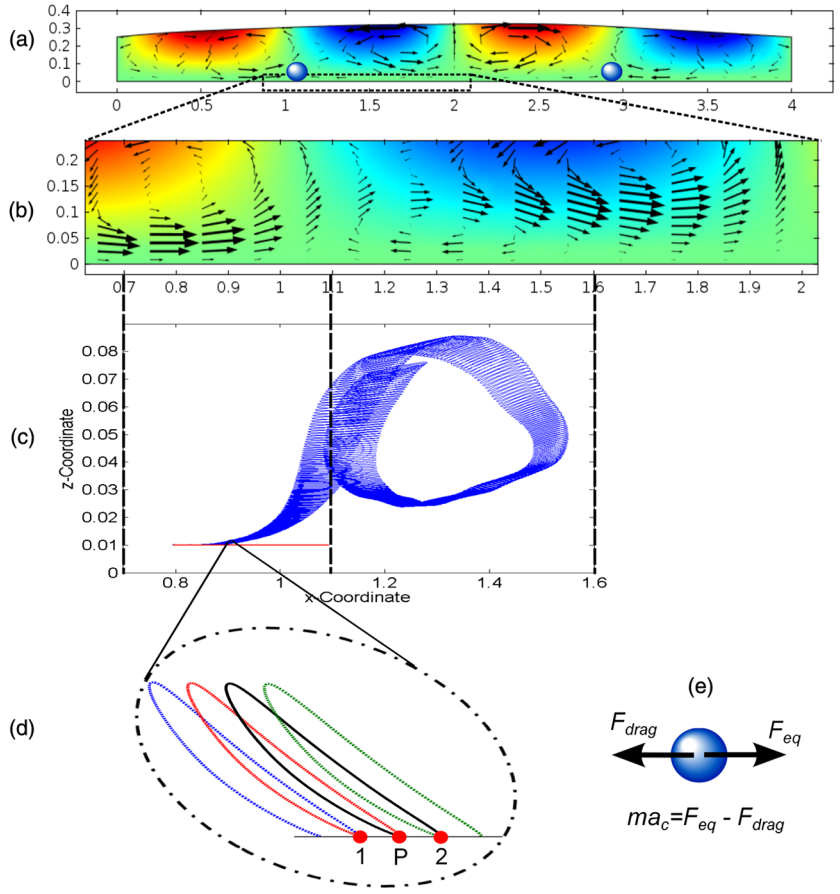

FIG. 6. (a) The w_1 field (contour plot) and the streaming vortices (arrow plot) for a chamber of dimensions $(L, h) = (4\text{ mm}, 0.25\text{ mm})$ vibrating at 220 Hz. The circles indicate the particle collection locations because of the first-order fields only. (b) Magnified view of the plots near the collection location. The surface plot shows the w_1 field as a reference for indication of nodal positions on the capillary wave. (c) Movement of a particle ($r = 10\ \mu$m, $\rho_p = 1500\text{ kg/m}^3$) towards the collection location (red) and motion of a particle ($r = 10\ \mu$m, $\rho_p = 1100\text{ kg/m}^3$) trapped in a streaming vortex (blue); the sum of the oscillatory motion due to first-order effects and the circulatory motion due to the second-order field can be seen. (d) The magnified movement of the particle [red particle in (c)] in the x direction over four cycles. Its motion over two cycles is analyzed to determine the equivalent force (F_{eq}) at point P in Sec. III A 2 a. (e) Forces on a particle in an alternate system used for calculating the equivalent force (F_{eq}): m is the mass of the particle, a_c is the acceleration, and F_{drag} is the drag force.

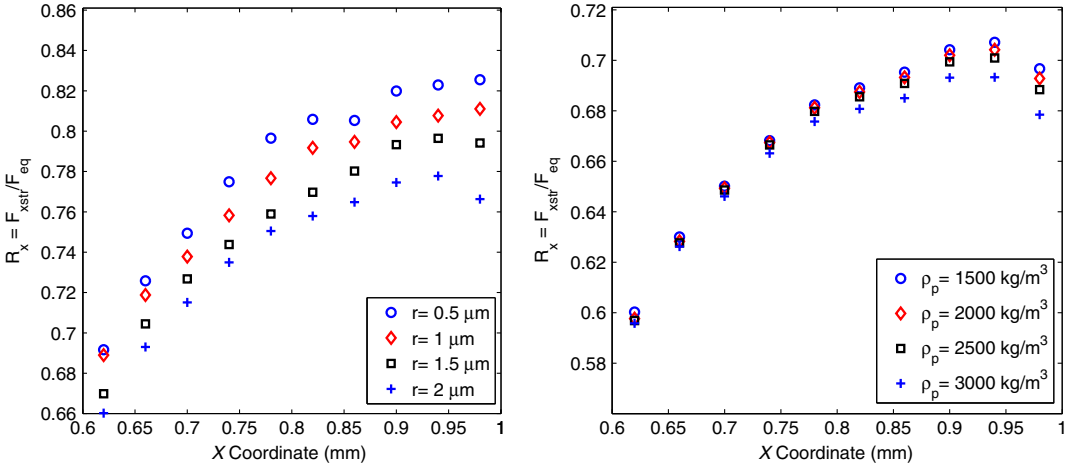

FIG. 7. Variation of the ratio (R_x) of the drag due to streaming (F_{xstr}) to the equivalent force (F_{eq}) on the particle in the x direction with varying (a) particle radius (r), $\rho_p = 4000\text{ kg/m}^3$; (b) particle density ($\rho_p$), $r = 5\ \mu$m. The data correspond to the motion of a particle in a chamber of dimensions $(L, h) = (4\text{ mm}, 0.25\text{ mm})$, vibrating at an amplitude 20 μm and frequency 220 Hz; this frequency corresponds to two wavelengths at the water-air interface. The particles collect at $x = 1.08$ mm.

The high value of R_x clearly suggests that the streaming field plays a significant contribution in the particle's net displacement, despite its magnitude being approximately 2 orders lower than the first-order fields. Furthermore, it is seen that the role of streaming is greater for particles of smaller size and density and, hence, lower inertia.

Simulations suggest that the u_2 field, in the region close to the base [Fig. 4(c)], increases linearly with distance from the base until the maximum value is reached. Following our assumption that the particles do not get dislodged from the base, and assuming that all forces act at the center of the particle, the u_2 field on the particle [i.e., u_S in Eq. (22)] will vary with r. Hence, $F_{x\mathrm{str}}$ will vary approximately as r^2, and, through simulations, F_{eq} is found to be varying as $r^{2.1}$. Therefore, the ratio (R_x) is proportional to $r^{-0.1}$. The increase in this ratio with decreasing particle size is also supported by the discussion in the previous section, that a particle with lower inertia will closely follow the motion of the fluid particle. As a result, the contribution of the first-order fields to the total displacement of the particle will decrease with decreasing particle radius. This also plays an important role in particle movement near the nodes X and Y (Fig. 4). The first-order field variations at these locations force the particles away, but the relatively weak streaming fields converge towards these locations. As the ratio R_x increases with decreasing particle radius, the streaming field can completely dominate the motion of sufficiently small particles and, therefore, induce collection at X and Y (this will be later observed experimentally in Sec. III B 2).

The effect of density on these forces is not very significant; nevertheless, $F_{x\mathrm{str}}$ varies as $\rho_p^{-0.04}$ and F_{eq} as $\rho_p^{0.01}$. Therefore, R_x varies as $\rho_p^{-0.05}$, which signifies a dominant streaming field with decreasing particle density. Hence, with a decrease in particle inertia, the influence of a streaming field on the particle's motion increases.

Particle motion in the z direction.—Up until now, we have considered the particle's motion only in the x direction; however, this is an artificial constraint in many cases—for example, it can be seen in the simulation data presented in Fig. 6(c) that particles can remain at the base of the chamber, but, in contrast, other particles can, in the same fluid flow field, circulate in the vortex and, as such, have a variation in location in both the x and z directions. We now consider the effects in the z direction, which dictate the transition between these two distinct behaviors.

Under the action of the first-order fields only, the particle's weight prevents it from getting vertically displaced over a cycle. However, a particle with sufficiently low inertia may get dislodged from the base momentarily; this happens when the upward drag due to the w_1 field overcomes the weight of the particle at any instant of time during its motion. However, the w_1 field gradients are not strong enough to vertically displace the particle over a cycle. In this regard, the w_2 field primarily acts in countering the particle weight and thereby increasing the chances of a particle lift-off from the base. Therefore, in a limiting case, it can be expected that particles can get lifted at positions where the w_2 field is maximum; from Fig. 4(d), this corresponds to the locations A, B, and C. Once a particle gets a net vertical displacement after a cycle, it enters a region of a stronger w_2 field and, therefore, gets trapped in the streaming vortices. This hinders collection of particles in stable locations, and, therefore, it is critical to assess the variation of the drag due to the w_2 streaming field with particle inertia.

As mentioned previously, the w_2 streaming field primarily counters the particle weight. Therefore, its effect on the particle's vertical movement can be estimated by considering the ratio (R_z) of the drag due to the w_2 field ($F_{z\mathrm{str}}$) with the buoyancy-corrected particle weight [F_b from Eq. (14b)] of a particle at point P. The drag due to w_2 field is given by

$$F_{z\mathrm{str}} = 6\pi\mu r w_S. \tag{23}$$

Here w_S is the w_2 field encountered by the particle at P (similar to u_S in the previous section). As with the u_2 field, the w_2 field also varies linearly in the z direction; therefore, $F_{z\mathrm{str}}$ varies roughly as r^2 (similar to $F_{x\mathrm{str}}$). As a result, the ratio $R_z = F_{z\mathrm{str}}/F_b$ varies with the particle radius as approximately r^{-1}. Similarly, R_z is inversely proportional to the particle density. Therefore, with a decrease in particle inertia, the tendency of a particle getting dragged vertically due to the w_2 field increases.

It is seen that a decrease in particle inertia increases the effect of both u_2 and w_2 streaming fields on the particle's motion. Having understood this inertial dependence of the streaming fields on the particle's net movement, we now investigate its effect by altering the flow properties; this is achieved by changing the chamber dimensions, i.e., length (L), depth (h), and actuation amplitude (A_0).

3. Variation of particle behavior with flow parameters

In the previous section, it was seen that the streaming field enhances the speed of collection in the x direction. However, if the streaming is too strong, then the particles will be dragged in the z direction and circulate in the streaming vortices. Therefore, for a given flow field, this upward translation of the particle offers the critical condition which will determine the minimum particle size or density, which can be collected in that fluid field. Therefore, for a given particle size and density, we will vary the parameters that dictate the flow properties, i.e., the chamber dimensions (L, h) and the actuation amplitude (A_0), with an aim to minimize the effect of streaming flows, even if this lowers the speed of collection in the x direction.

Simulation results have been presented by varying each of these parameters (A_0, L, h) individually across the range as mentioned in Table I, while the other parameters are kept constant at the specified "base value."

TABLE I. Range of flow parameters considered for the streaming force analysis. The capillary wave at the interface is of two wavelengths in all the simulations.

Parameter	Range	Base value
A_0	20–40 μm	25 μm
L	3–7 mm	4 mm
h	0.1–0.3 mm	0.25 mm

Similar to the analysis in Secs. III A 2 a and III A 2 b, we are interested in observing the dependence of R_x and, primarily, R_z on these flow-defining parameters; the subsequent variations are tabulated in Table II.

The streaming fields originate because of the action of a time-averaged body force, depending on the gradients of the first-order fields [Eq. (10)]. Therefore, in general, it can be expected that an increase in the velocity field gradients will increase this time-averaged body force and, hence, will lead to stronger streaming fields. An increase in the vibration amplitude directly increases the first-order field gradients, which results in the positive exponents for $F_{x\mathrm{str}}$ and $F_{z\mathrm{str}}$ in Table II. Another method to increase these gradients is by decreasing the boundary layer thickness, i.e., by increasing the resonant frequency of the system. Therefore, for a fixed vibration mode, an increase in the chamber height (h) or a decrease in the chamber length (L) would increase the resonant frequency of the system [Eq. (7)] and, hence, the increased streaming forces. As the particle weight is independent of any changes in the flow, R_z follows the same variation as $F_{z\mathrm{str}}$, in Table II. This result implies an increase in R_z with increased streaming forces, thereby increasing the possibility of a particle lift-off from the base.

It is established in Sec. III A 2 b that once a particle encounters a vertical displacement over a cycle, it is deemed to follow the streaming trajectory, and if the lift-off does not occur, then the particle will be collected at a stable location. A chamber, with a given geometry, when vibrated at a given vibration amplitude, will have a specific flow field which would be capable of lifting particles below a certain value of its size or density; the corresponding set of values of the particle radius and density are referred to as the "cutoff" values. This also implies that any particle with a higher radius or density than the set of cutoff values will not be lifted into the swirling patterns and, hence, will get collected at stable locations. Therefore, for a given flow field, it is desirable to have lower cutoff values.

TABLE II. The variation of collection and streaming forces with the flow parameters. The exponents b, in the format $Y \propto X^b$, are listed below. $R_x = F_{x\mathrm{str}}/F_{\mathrm{eq}}$ and $R_z = F_{z\mathrm{str}}/F_b$.

	Horizontal actuation (X)		
Y	A_0	h	L
F_{eq}	2.5	−0.1	−2.5
$F_{x\mathrm{str}}$	2.2	0.1	−2.9
$F_{z\mathrm{str}}$	2.0	1.3	−4.7
R_x	−0.3	0.2	−0.4
R_z	2.0	1.3	−4.7

By reducing the streaming effects in the z direction, we seek to minimize the cutoff, thereby allowing the collection of very small particles. Such a modification will also decrease streaming forces in the x direction, but it is of little significance, as this effect can be compensated by an increase in the experiment run time. We calculate this set of particle cutoff values for the different cases listed in Table I. The lowest value of particle density is found against a range of particle radii (2–10 μm), such that the particle encounters zero displacement in the vertical direction over a cycle. As the tendency of particle lift-off is maximum close to the collection location (Sec. III A 2 b), the particle's vertical displacement over a cycle is measured in the region close to it. The corresponding cutoff values are plotted in Fig. 8.

The plots in Fig. 8 reiterate the trends presented in Table II, that the cutoff values will decrease by reducing the streaming in the z direction (i.e., $F_{z\mathrm{str}}$ or R_z); this is possible by decreasing the vibration amplitude and chamber height and by increasing the chamber length. The three cases have been consolidated through Eq. (24):

$$\frac{A_0^2}{\lambda}\left(\frac{h}{\lambda}\right)^{0.9}\left[\frac{1}{\lambda}\left(\frac{\gamma}{\rho_0 g}\right)^{0.25}\right]^{2.2} = 63.4\frac{\rho_p-\rho_0}{\rho_0}r. \quad (24)$$

The above equation is plotted in Fig. 9, where Y signifies the flow conditions and X is the inertial parameter:

$$Y = \frac{A_0^2}{\lambda}\left(\frac{h}{\lambda}\right)^{0.9}\left[\frac{1}{\lambda}\left(\frac{\gamma}{\rho_0 g}\right)^{0.25}\right]^{2.2}, \quad (25a)$$

$$X = \frac{\rho_p-\rho_0}{\rho_0}r. \quad (25b)$$

Here $\lambda = L/n$ is the capillary wavelength at the interface, where n is the number of capillary waves (or the mode number); in the present simulations, $n = 2$; therefore, $\lambda = L/2$. However, it is to be mentioned here that Eq. (24) holds true only for $n = 2$. For other higher modes, the proportionality constant between Y and X will change. This is so because at the mode $n = 2$, the streaming field under one wave will be affected by the velocity gradients due to the no-slip condition at the side walls. As the mode number increases, the capillary waves, which are further away from the side walls (or closer to the center of the chamber), will be less affected by these side wall gradients. As a result, the streaming forces near the center of the chamber will be less than those near the walls. In such a case, particle sizes closer to the cutoff value will collect near the center, rather than near the side walls. However, due to the decrease in λ, the cutoff values will still be higher

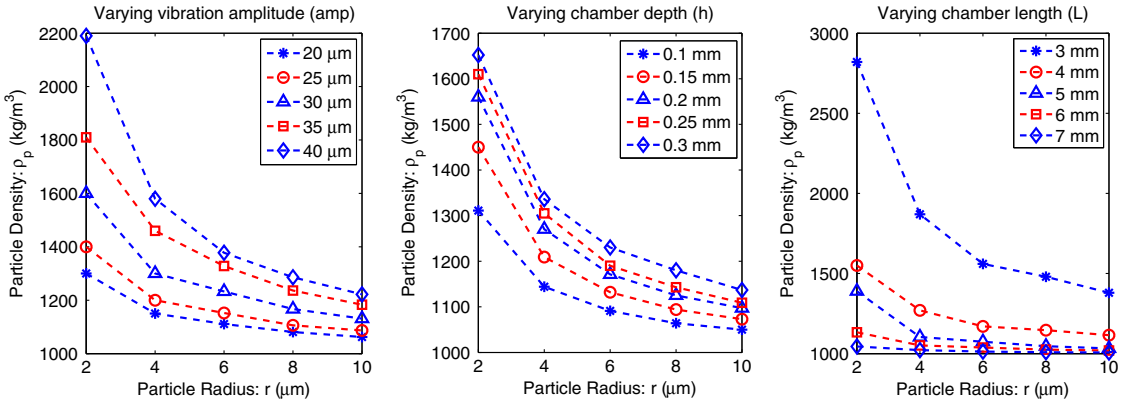

FIG. 8. Variation of the set of cutoff values for particle radius and density with varying (a) vibration amplitude, (b) chamber depth, and (c) chamber length.

than the lower modes, but the difference will be slightly less than that obtained through Eq. (24). Therefore, in Eq. (24), the proportionality constant will be a function of the mode number.

Reverting to Fig. 9, for a fixed Y, i.e., for a given chamber size and vibration amplitude, any point to the right of the fit curve will correspond to a particle with a higher inertia than the cutoff value; therefore, it will accumulate at the respective collection location, whereas a point on the left will correspond to a particle swirling in the streaming flows. We now use these data to track the collection of particles with changing flow parameters for the experimental results.

B. Experiments

It is demonstrated in Sec. III A 3, through simulations, that a chamber with smaller depth, vibrating with a higher capillary wavelength at lower amplitudes, will reduce the cutoff inertia value and enable particle collection in stable locations. Using Eq. (24), we now track the above changes through experimental data. However, in comparing the simulation data with experiments, it is to be realized that certain assumptions are imposed on particle motion in the simulations, such as the presence of particles does not affect the flow field, the forces act at the center of the particle, and the particle undergoes only a translation motion (i.e., no rotation). Furthermore, the 2D simulations assume an unbounded fluid in the y direction, which is not the case in reality; the side walls forming the width of the chamber will add to the viscous damping. This will lower the capillary wave amplitude slightly, thereby reducing the flow-field gradients experienced by the particle. Therefore, a certain disparity between the simulation and experimental results will be present. Nevertheless, the simulation results provide a fair estimate of the experimental cutoff values, as will be seen the following discussion.

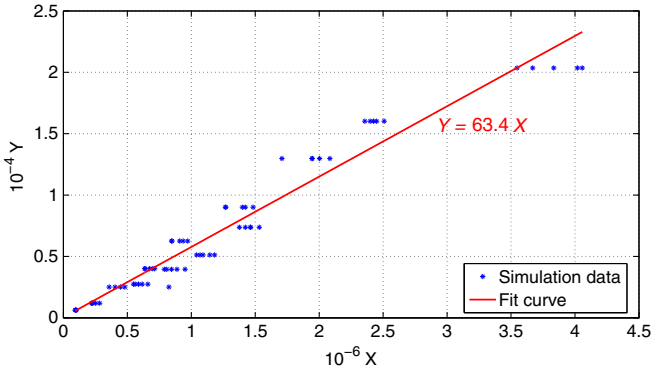

FIG. 9. Plots of data and fit curve given by Eq. (24) indicating the lowest particle properties for zero vertical displacement of the particle. The fit curve is given by the equation $Y = (63.4)X$, where Y and X are given by Eqs. (25a) and (25b), respectively.

1. Changes in chamber dimensions

We first take the case of silica particles of diameter 1 μm and density 2000 kg/m^3 ($X = 5 \times 10^{-7}$) and track the changes in the chamber dimension required for a stable collection, by calculating Y and plotting in Fig. 10(a).

The value of Y is traced from the experimental conditions in Fig. 11(a) to the conditions in Fig. 11(b). In this analysis, only the effect of chamber geometry is explored; i.e., the vibration amplitude is kept constant throughout.

Although the results are presented for different modes, we still use Eq. (24) for the analysis, assuming that the proportionality constant does not change drastically with a mode change from 2 to 3. It is to be mentioned that, in Fig. 10(a), the value of Y, for a given chamber size and vibration amplitude, should be lower than Y_c to ensure a stable collection.

The starting point (point 1) is a chamber with dimensions $(L, h) = (4\text{ mm}, 0.25\text{ mm})$ vibrating with two capillary wavelengths at the interface ($\lambda = 2$ mm), corresponding to Fig. 11(a). Here, the value of Y is higher than Y_c, which implies that the particles should not collect underneath the alternate nodes. However, in Fig. 11(a), a faint collection is visible. This collection is attributed to the difference in simulation and experimental results mentioned previously. In any case, a further reduction in Y is explored to obtain a

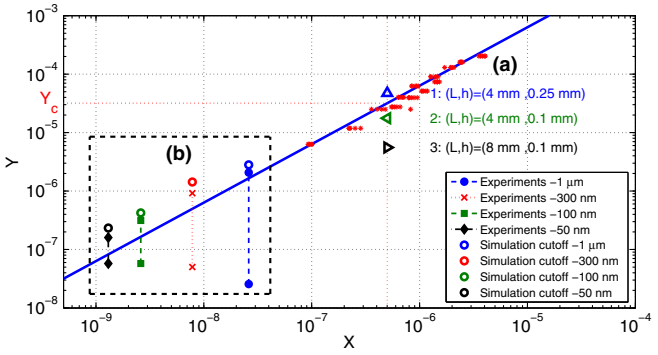

FIG. 10. Plot of the cutoff curve $Y = (63.4)X$; the simulation data points (from Fig. 9) are indicated as red dots. (a) Tracking changes for changing the chamber dimensions for collecting 1-μm silica particles at constant amplitude (for the study in Sec. III B 1). Y_c is the critical value of the flow parameters corresponding to the 1-μm silica particles. For a given chamber size, the condition $Y < Y_c$ should be satisfied for obtaining a collection. (b) Plot of values of Y for collecting polystyrene particles of different sizes in a chamber of dimension $(L, h) = (8\ \text{mm}, 0.1\ \text{mm})$ vibrating with six capillary wavelengths (for the study in Sec. III B 2). λ and h being constant, the upper and lower points are the values of Y corresponding to the maximum and minimum vibration amplitude capable of collecting the respective polystyrene particles. The hollow spheres are the critical values of Y for the corresponding particle sizes in the same chamber and frequency.

better collection. A reduction in height of the fluid volume is proven effective in collecting 100-nm particles in vertically vibrating drops [43]. Following this, keeping the mode number same, the chamber depth is decreased to $h = 0.1$ mm [point 2 in Fig. 10(a)]. Finally, to simulate the conditions of Fig. 11(b), the chamber length is increased to 8 mm, and the mode number is changed to 3 ($\lambda = 2.67$ mm). It is clear from Fig. 10(a) that the value of Y for this case (point 3) is well below Y_c. Experimentally,

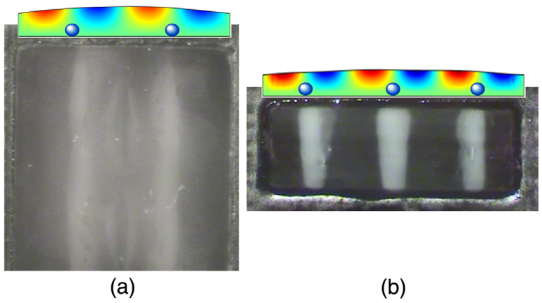

FIG. 11. Comparison of collection of 1-μm silica particles (density $= 2000\ \text{kg/m}^3$) in horizontally actuated chambers of different dimensions: (a) $(L, h) = (4\ \text{mm}, 0.25\ \text{mm})$ at 220 Hz; (b) $(L, h) = (8\ \text{mm}, 0.1\ \text{mm})$ at 104 Hz. w_1 field from COMSOL simulations are shown for indicating the nodal positions on the capillary wave. The blue circles represent the collection locations. The chambers are vibrated with an amplitude of approximately 20 μm.

this result is reflected in the difference in quality of collection in Figs. 11(a) and 11(b).

Following the above results, chambers of length 8 mm and depth 0.1 mm are used for further experiments. A further change in the vibration amplitude will correspond to a point on the vertical dotted line in Fig. 10(a) and will ensure a collection, till the condition $Y < Y_c$ is satisfied. Therefore, the vibration amplitude is adjusted as experiments proceed, ensuring that a discernible collection pattern is observed before the water evaporates. After observing the corelation between the simulation results and experimental data for changing flow parameters, we now explore the limits of this system by collecting particles with a further lower inertia.

2. *Collection of submicron-sized polystyrene particles*

For collecting particles with lower inertia, evaporation of water plays a critical role. Because of their low inertia, the particles take time to move towards the collection region. This increased collection time is acceptable until a certain limit, as in the absence of a humidity-controlled environment, evaporation of water places a constraint on the experiment run time. This has two implications: (a) the entire volume of water might evaporate before any collection is observed, and (b) due to the change in the volume of water, the resonant frequency of the capillary wave changes.

To overcome this constraint, two methods are employed. First, the chamber is overloaded with water (about 4 μl is used for the current experiments), so as to extend the experiment run time. For this case, the resonant frequency of a capillary wave of six wavelengths is approximately 330 Hz, whereas that when the interface is almost flat is approximately 350 Hz; as water evaporates, the resonant frequency will increase from 330 Hz. Hence, it is necessary to find the optimum frequency value for which particle collection will be observed for the entire duration of the experiment. Prior to collecting the data in Fig. 10(b), a number of experiments are carried out to find the frequency at which these particles are seen to collect in lines after about 3 min of actuation; this frequency is found to be about 336 Hz for a 4-μl initial volume of water.

Second, the chamber is vibrated at a higher mode, in this case, at mode 6. To provide a comparison for the collection times for different mode numbers (at the same cutoff particle size), let us assume a particle at a distance 0.1λ from the collection location. If, in one cycle (i.e., in time $1/f$), the particle travels a distance Δx, then the time taken to cover the distance 0.1λ can be estimated to be proportional to $\lambda(1/f)/\Delta x$. The term $\Delta x/(1/f)$ is roughly equivalent to the collection force F_{eq} [Eq. (20)]; therefore, the collection time is proportional to λ/F_{eq}.

By increasing the mode number (for instance, from $m = 1$ to $m = 6$), a decrease in the capillary wavelength will increase the collection force but also increase the

streaming field and, therefore, the cutoff value. However, in the case of a wavelength variation due to a change in mode number, the cutoff value variation is less drastic than that obtained from Eq. (24), as explained in Sec. III A 3. Nevertheless, with the above mode change, the cutoff value will still increase. To bring this cutoff down to the same value as at $m = 1$, the vibration amplitude has to be decreased. As a result of this, overall, F_{eq} might decrease. However, as λ also decreases with increasing mode number, the collection time (which is proportional to λ/F_{eq}) can follow either trend with an increasing mode number. Through experiments, it is seen that the collection time decreases with increasing mode number, as collection of lighter particles at lower modes is hardly visible, during the experiment run time. The mode $m = 6$ is found to give the best collection before the water evaporates.

Finally, having fixed the capillary wavelength and the chamber depth, the vibration amplitude is found through repeated trials. As mentioned earlier, the upper and lower extents of the vibration amplitude are restricted by the critical value Y_c and the experiment run time, respectively. This band of acceptable actuation amplitudes is found experimentally for each of the particles in Fig. 12. This range of amplitudes is plotted through Y in Fig. 10(b), for comparison with simulation results represented through the fit curve. In ideal conditions, the upper bound should approximately coincide with the fit curve, but this disparity is due to the assumptions imposed on the particle motion in the simulations and the change in mode number; the change in mode number affects the proportionality constant between X and Y in Eq. (24).

It is noteworthy to mention that the initial volume of water inserted in the chamber is critical. With a lower volume, the experiment run time is restricted, which results in a narrow amplitude range over which collection is observed. With a higher volume of water, the amplitude range does not change significantly, but the experiment run time has to be increased to observe any collection. After repeated experiments with different volumes of water, the widest amplitude range was observed with a 4-μl water volume.

The collection patterns observed for these particle sizes are different from that obtained in Fig. 11(b). This difference can be explained from the negative exponent value for R_x with particle inertia (Sec. III A 2 a) and vibration amplitude (Table II). The negative exponent value for both the parameters corresponds to an increased contribution of the streaming forces with decreasing particle radius (r) and vibration amplitude (A_0), respectively. As explained in Sec. III A 2 a, this change will not affect the particle movement at the nodes A, B, and C (Fig. 4) but will increase the tendency of the streaming field to dominate the particle's motion and force it to converge underneath the nodes corresponding to positions X and Y in Fig. 4.

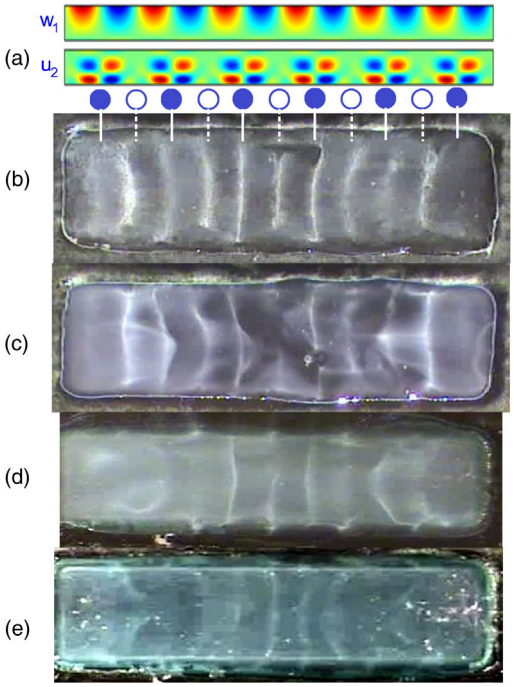

FIG. 12. Collection of polystyrene particles ($\rho_p = 1050\ \mathrm{kg/m^3}$) of varying sizes in the chamber of dimensions $(L, h) = (8\ \mathrm{mm}, 0.1\ \mathrm{mm})$ vibrating with six wavelengths at the interface at 336 Hz. (a) COMSOL plots for w_1 (top) and u_2 (bottom) fields for six wavelengths of the capillary wave. The w_1 plot is shown to discern the position of nodes on the capillary wave. The u_2 plot is indicated as a reference for the collection locations. The collection locations indicated by the solid circles correspond to collection at positions A, B, and C in Fig. 4, and those indicated by the hollow circles correspond to collection at positions X and Y; (b) 1 μm; (c) 300 nm; (d) 100 nm; (e) 50 nm.

IV. CONCLUSION

The streaming phenomenon due to first-order velocity gradients is explored in rectangular chambers, undergoing low-frequency horizontal vibrations. A perturbation scheme is used to formulate the second-order governing equations for the flow. The first- and second-order fields are simulated, and particle motion is studied in the superimposed fields. The particle's motion can be roughly split into two components, whereby it is found that the streaming field dominates the particle's displacement over a cycle. Furthermore, with the aim of reducing streaming, cutoff particle parameters are obtained for various chamber configurations and vibration amplitudes. It is found that a longer capillary wavelength, in a chamber with a small depth, when vibrated at low amplitudes, provides the least streaming, or, in other words, particles with low inertia can be collected. This result is validated through experiments, where a drastic reduction in the streaming due to an increased chamber length is observed. However, such modifications also reduce the collection force (F_{eq}), which increases the collection time. This increase hinders the

collection of particles with lower inertia, as the experiment run time (constrained by the evaporation of the entire volume of water) interferes with the collection time. This constraint is experimentally resolved by employing a higher vibration mode of the capillary wave. As a result, particles as low as 50 nm in diameter (and density 1050 kg/m^3) are collected underneath the nodes of the capillary wave.

ACKNOWLEDGMENTS

The authors thank the Australian Research Council through Discovery Grant No. DP110104010 for their kind support of this research.

[1] C. Zhang, K. Khoshmanesh, A. Mitchell, and K. Kalantar-zadeh, Dielectrophoresis for manipulation of micro/nano particles in microfluidic systems, Anal. Bioanal. Chem. **396**, 401 (2010).
[2] C. Mio, T. Gong, A. Terray, and D. W. M. Marr, Design of a scanning laser optical trap for multiparticle manipulation, Rev. Sci. Instrum. **71**, 2196 (2000).
[3] Q. Cao, X. Han, and L. Li, Two-dimensional manipulation of magnetic nanoparticles in microfluidic systems, Appl. Phys. Express **6**, 025201 (2013).
[4] A. Garcia-Sabaté, A. Castro, M. Hoyos, and R. González-Cinca, Experimental study on inter-particle acoustic forces, J. Acoust. Soc. Am. **135**, 1056 (2014).
[5] L. P. Gor'kov, On the forces acting on a small particle in an acoustical field in an ideal fluid, Sov. Phys. Dokl. **6**, 773 (1962).
[6] A. A. Doinikov, Acoustic radiation pressure on a compressible sphere in a viscous fluid, J. Fluid Mech. **267**, 1 (1994).
[7] J. J. Hawkes and W. T. Coakley, Force field particle filter, combining ultrasound standing waves and laminar flow, Sens. Actuators, B **75**, 213 (2001).
[8] D. A. Johnson and D. L. Feke, Methodology for fractionating suspended particles using ultrasonic standing wave and divided flow fields, Sep. Technol. **5**, 251 (1995).
[9] D.-C Seo, A. K. M. A. H. Siddique, B. Ahn, C. Kim, and S. Cho, Ultrasonic flow-through filtration of microparticles in a microfluidic channel using frequency sweep technique, J. Mech. Sci. Tech. **27**, 825 (2013).
[10] E. J. Fong, A. C. Johnston, T. Notton, S.-Y Jung, K. A. Rose, L. S. Weinberger, and M. Shusteff, Acoustic focusing with engineered node locations for high-performance microfluidic particle separation, Analyst **139**, 1192 (2014).
[11] A. Nilsson, F. Petersson, H. Jonsson, and T. Laurell, Acoustic control of suspended particles in micro fluidic chips, Lab Chip **4**, 131 (2004).
[12] S. Oberti, D. Moeller, A. Neild, J. Dual, F. Beyeler, B. J. Nelson, and S. Gutmann, Strategies for single particle manipulation using acoustic and flow fields, Ultrasonics **50**, 247 (2010).
[13] A. L. Bernassau, P. Glynne-Jones, F. Gesellchen, M. Riehle, M. Hill, and D. R. S. Cumming, Controlling acoustic streaming in an ultrasonic heptagonal tweezers with application to cell manipulation, Ultrasonics **54**, 268 (2014).
[14] A. Neild, S. Oberti, G. Radziwill, and J. Dual, Simultaneous positioning of cells into two-dimensional arrays using ultrasound, Biotechnol. Bioeng. **97**, 1335 (2007).
[15] O. Manneberg, B. Vanherberghen, J. Svennebring, H. M. Hertz, B. Önfelt, and M. Wiklund, A three-dimensional ultrasonic cage for characterization of individual cells, Appl. Phys. Lett. **93**, 063901 (2008).
[16] J. Greenhall, F. G. Vasquez, and B. Raeymaekers, Continuous and unconstrained manipulation of micro-particles using phase-control of bulk acoustic waves, Appl. Phys. Lett. **103**, 074103 (2013).
[17] P. Glynne-Jones, R. J. Boltryk, N. R. Harris, A. W. J. Cranny, and M. Hill, Mode-switching: A new technique for electronically varying the agglomeration position in an acoustic particle manipulator, Ultrasonics **50**, 68 (2010).
[18] A. L. Bernassau, C. R. P. Courtney, J. Beeley, B. W. Drinkwater, and D. R. S. Cumming, Interactive manipulation of microparticles in an octagonal sonotweezer, Appl. Phys. Lett. **102**, 164101 (2013).
[19] S. Oberti, A. Neild, R. Quach, and J. Dual, The use of acoustic radiation forces to position particles within fluid droplets, Ultrasonics **49**, 47 (2009).
[20] R. Jensen, I. Gralinski, and A. Neild, Ultrasonic manipulation of particles in an open fluid film, IEEE Trans. Ultrason. Ferroelectr. Freq. Control **60**, 1964 (2013).
[21] W. L. M. Nyborg, *Physical Acoustics IIB* (Academic, New York, 1965), p. 265.
[22] C. Eckart, Vortices and streams caused by sound waves, Phys. Rev. **73**, 68 (1948).
[23] M. Wiklund, R. Green, and M. Ohlin, Acoustofluidics 14: Applications of acoustic streaming in microfluidic devices, Lab Chip **12**, 2438 (2012).
[24] P. B. Muller, R. Barnkob, M. J. H. Jensen, and H. Bruus, A numerical study of microparticle acoustophoresis driven by acoustic radiation forces and streaming-induced drag forces, Lab Chip **12**, 4617 (2012).
[25] J. Lei, P. Glynne-Jones, and M. Hill, Acoustic streaming in the transducer plane in ultrasonic particle manipulation devices, Lab Chip **13**, 2133 (2013).
[26] J. Lei, M. Hill, and P. Glynne-Jones, Numerical simulation of 3d boundary-driven acoustic streaming in microfluidic devices, Lab Chip **14**, 532 (2014).
[27] P. B. Muller, M. Rossi, Á. G. Martin, R. Barnkob, P. Augustsson, T. Laurell, C. J. Kähler, and H. Bruus, Ultrasound-induced acoustophoretic motion of microparticles in three dimensions, Phys. Rev. E **88**, 023006 (2013).
[28] K. Sritharan, C. J. Strobl, M. F. Schneider, A. Wixforth, and Z. Guttenberg, Acoustic mixing at low reynolds numbers, Appl. Phys. Lett. **88**, 054102 (2006).
[29] G. G. Yaralioglu, I. O. Wygant, T. C. Marentis, and B. T. Khuri-Yakub, Ultrasonic mixing in microfluidic channels using integrated transducers, Anal. Chem. **76**, 3694 (2004).
[30] M. Ohlin, A. E. Christakou, T. Frisk, B. Önfelt, and M. Wiklund, Influence of acoustic streaming on ultrasonic particle manipulation in a 100-well ring-transducer microplate, J. Micromech. Microeng. **23**, 035008 (2013).
[31] M. Hoyos and A. Castro, Controlling the acoustic streaming by pulsed ultrasounds, Ultrasonics **53**, 70 (2013).
[32] P. Rogers, I. Gralinski, C. Galtry, and A. Neild, Selective particle and cell clustering at airliquid interfaces within

ultrasonic microfluidic systems, Microfluid. Nanofluid. **14**, 469 (2013).

[33] C. Devendran, I. Gralinski, and A. Neild, Separation of particles using acoustic streaming and radiation forces in an open microfluidic channel, Microfluid. Nanofluid. **17**, 879 (2014).

[34] L. A. Kuznetsova and W. T. Coakley, Applications of ultrasound streaming and radiation force in biosensors, Biosens. Bioelectron. **22**, 1567 (2007).

[35] F. Zoueshtiagh, P. J. Thomas, V. Thomy, and A. Merlen, Micrometric granular ripple patterns in a capillary tube, Phys. Rev. Lett. **100**, 054501 (2008).

[36] R. Wunenburger, V. Carrier, and Y. Garrabos, Periodic order induced by horizontal vibrations in a two-dimensional assembly of heavy beads in water, Phys. Fluids **14**, 2350 (2002).

[37] D. Leighton and A. Acrivos, The shear-induced migration of particles in concentrated suspensions, J. Fluid Mech. **181**, 415 (1987).

[38] S. Lukaschuk, P. Denissenko, and G. Falkovich, Nodal patterns of floaters in surface waves, Eur. Phys. J. Spec. Top. **145**, 125 (2007).

[39] P. Agrawal, P. S. Gandhi, and A. Neild, The mechanics of microparticle collection in an open fluid volume undergoing low frequency horizontal vibration, J. Appl. Phys. **114**, 114904 (2013).

[40] P. Agrawal, P. S. Gandhi, and A. Neild, Quantification and comparison of low frequency microparticle collection mechanism in an open rectangular chamber, J. Appl. Phys. **115**, 174505 (2014).

[41] J. Whitehill, A. Neild, T. W. Ng, and M. Stokes, Collection of suspended particles in a drop using low frequency vibration, Appl. Phys. Lett. **96**, 053501 (2010).

[42] M. S. Longuet-Higgins, Mass transport in water waves, Phil. Trans. R. Soc. A **245**, 535 (1953).

[43] J. D. Whitehill, I. Gralinski, D. Joiner, and A. Neild, Nanoparticle manipulation within a microscale acousto-fluidic droplet, J. Nanopart. Res. **14**, 1223 (2012).

[44] L. D. Landau and E. M. Lifshitz, *Fluid Mechanics* (Pergamon, Oxford, 1987), p. 247.

[45] R. Clift, J. R. Grace, and M. E. Weber, *Bubbles, Drops and Particles* (Academic, New York, 1978).

[46] J. F. Richardson, J. H. Harker, and J. R. Backhurst, *Particle Technology and Separation Processes* (Butterworth Heinemann, Woburn, MA, 2002), p. 153.

[47] A. J. Goldman, R. G. Cox, and H. Brenner, Slow viscous motion of a sphere parallel to a plane wallii couette flow, Chem. Eng. Sci. **22**, 653 (1967).

[48] B. A. Puthenveettil and A. J. Hopfinger, Evolution and breaking of parametrically forced capillary waves in a circular cylinder, J. Fluid Mech. **633**, 355 (2009).

[49] L. Rayleigh, On the circulation of air observed in kundt's tubes, and on some allied acoustical problems, Phil. Trans. R. Soc. London **175**, 1 (1884).